Earth and Planetary Science Letters 601 (2023) 117905

Contents lists available at ScienceDirect

Earth and Planetary Science Letters

journal homepage: www.elsevier.com/locate/epsl

Towards ground motion prediction for potential large earthquakes from interseismic locking models

Suli Yao, Hongfeng Yang *

Earth and Environmental Sciences Programme, The Chinese University of Hong Kong, Shatin, Hong Kong, China

ARTICLE INFO

Article history:
Received 11 July 2022
Received in revised form 15 October 2022
Accepted 2 November 2022
Available online 21 November 2022
Editor: J.P. Avouac

Dataset link: https://www.unavco.org/data/gps-gnss/gps-gnss.html

Dataset link: http://www.lis.ucr.ac.cr

Keywords:
interseismic locking models
dynamic rupture scenarios
synthetic ground motions
2012 Nicoya Mw 7.6 earthquake

ABSTRACT

Interseismic locking models derived from geodetic data describe slip deficit accumulation on faults, hence indicating the likelihood of future earthquakes. In recent years, locking models have been used to develop dynamic scenarios for potential large earthquakes. However, whether those scenarios are effective in representing the rupture process and ground motion intensity in future earthquakes remains unclear. In this study, we examine the ground motion predictions in locking-based dynamic rupture scenarios by comparing them with the predictions from ground motion models (GMMs) and the observations in a real earthquake. We utilize two locking models as constraints on the stress heterogeneity and obtain synthetic ground motion measures, including the peak ground velocity (PGV) and the peak ground displacement (PGD), through conducting dynamic rupture simulations for M7 earthquakes on the Nicoya megathrust. The predictions are generally consistent with GMMs with some differences in attenuation rate and amplitude in the near field ($<$ 30 km). However, the spatial patterns differ a lot from GMM-based predictions, mainly due to the rupture directivity effect. By comparing with scenarios under homogenous stress conditions, we observe the dependency of earthquake magnitude and rupture directivity on stress heterogeneity. The coseismic slip appears to negatively correlate with stress roughness. Furthermore, the predictions from one locking model capture most of the measurements on the local network during the 2012 Nicoya Mw 7.6 earthquake. Our results underline the necessity of involving rupture dynamics and stress heterogeneities in prescribing the earthquake source and highlight the potential application of locking models in seismic hazard assessment.

1. Introduction

Recent advances in geodetic monitoring have enabled interseismic locking models to be developed that reveal the distribution of the slip deficit build-up rate on faults. These models have significantly advanced our understanding of future earthquake potential. In general, highly locked regions are anticipated to hold significant coseismic slip in future earthquakes, and this intuition has been vindicated in several cases, including the 2010 Mw 8.8 Maule, the 2012 Mw 7.6 Nicoya, the 2015 Mw 7.8 Gorkha, and the 2022 Mw 6.6 Menyuan earthquakes (Satake and Atwater, 2007; Moreno et al., 2010; Métois et al., 2013; Perfettini et al., 2010; Protti et al., 2014; Avouac et al., 2015; Yang et al., 2022). Some studies suggest using slip deficit as an approximation of coseismic slip in future earthquakes (e.g. Baranes et al., 2018). However, the uncertainty can be considerable, partly due to the difficulty in precisely quantifying the slip deficit prior to an earthquake considering temporal changes in locking depth (Bruhat and Segall, 2017), the build-up and release rate of slip deficit (Yang et al., 2019b), and the uncertainty caused by the elastic-earth assumption (Wang et al., 2021). Moreover, locking models usually suggest heterogeneous stress accumulation patterns with multiple segments. The observed rupture segmentation, such as along the locked Chile margin, as well as the results of numerical rupture simulations, indicates high complexities in the final extent of earthquakes and rupture propagation processes that cannot be solely constrained by static locking models (Hok et al., 2011; Ader et al., 2012; Chlieh et al., 2011; Yu et al., 2018; Yang et al., 2019a). There is still some doubt, therefore, on how to derive reliable information for seismic hazard assessment from interseismic locking models.

One approach to evaluating potential rupture process and extent for future earthquakes from locking models is deriving dynamic scenarios through spontaneous rupture simulations, in which the locking models are utilized to constrain the stress build-up patterns on faults. Given reasonable inputs for fault geometry, material properties, and friction properties, such dynamic scenarios can provide physically plausible rupture process, and have been

* Corresponding author.
E-mail address: hyang@cuhk.edu.hk (H. Yang).

https://doi.org/10.1016/j.epsl.2022.117905
0012-821X/

conducted in certain regions such as the Nankai Trough (Hok et al., 2011), the Cascadia subduction zone (Yang et al., 2012a; Ramos et al., 2021; Chan et al., 2022), the Nicoya megathrust (Yang et al., 2019b), and the Anninghe strike-slip fault in southwest China (Yao and Yang, 2022). However, it has not been possible to validate the scenarios with real earthquakes for most cases, due to the lack of instrumental records for large earthquakes except for the Nicoya megathrust. By nucleating ruptures from the hypocenter of the 2012 Mw 7.6 event, Yang et al. (2019b) have generated locking-based dynamic rupture scenarios that hold similar final slip distribution, moment rate function, and moment magnitude with finite fault rupture models of the 2012 Mw 7.6 event, which highlights the potential effectiveness of locking-based dynamic rupture scenarios as a tool in earthquake potential assessment.

In addition to the earthquake source process, quantitative seismic hazard assessment further demands accurate ground motion predictions, which are mostly conveyed through empirical ground motion models (GMMs) (Atkinson and Boore, 1995; Boore and Atkinson, 2008; Bindi et al., 2011). In these models, ground motion intensity measures (IM) are expressed as functions of a list of predictor variables related to earthquake sources and earth structures. However, GMMs often suffer from poor constraints in near-fault regions for large earthquakes due to inadequate data. In the past two decades, physics-based simulators (PBS), such as dynamic rupture simulators, have been applied to model rupture propagation and ground motions. The obtained predictions are comparable to (Olsen et al., 2006; Ripperger et al., 2008; Bydlon et al., 2019; Zhang et al., 2017), or even superior than, those from GMMs (Bradley et al., 2017; Bradley, 2019). Compared to GMMs, PBSs feature advantages in reflecting the impacts of complex physical processes in source and wave propagation such as the rupture directivity effect and the amplification in sediment basins (Bradley, 2019; Xin and Zhang, 2021).

The predictions from PBSs are well-known to highly depend on model inputs including the fault geometry, the material property, the frictional property, and the stress condition on faults (Harris, 2004). How to tune those parameters becomes critical. Due to the lack of direct measurements, the distribution of initial stress is poorly constrained and has often been assumed to be uniform, depth-dependent, stochastic, or dependent on the fault geometry (Olsen et al., 2006; Ripperger et al., 2008; Bydlon et al., 2019; Zhang et al., 2017). In addition, the rupture process itself is indeterministic, which poses uncertainties in ground motions. For instance, given the same initial condition, earthquakes with different hypocenters can result in diverse rupture directivities, rupture extents, and final magnitudes (Yang et al., 2019a; Yao and Yang, 2022; Xin and Zhang, 2021). Without sufficient prior knowledge of the hypocenter location, considering all potential nucleation sites is a viable way to quantify the uncertainties introduced by rupture indeterminism (Yang et al., 2019a; Yao and Yang, 2022).

Our study region is the Nicoya megathrust in Costa Rica. In Sep 2012, a Mw 7.6 earthquake occurred on the Nicoya megathrust (Protti et al., 2014). There are two locking models (Xue et al., 2015; Feng et al., 2012) derived based on geodetic data before the 2012 event (Fig. 1). This study aims to understand and validate the contribution of involving locking models and dynamic rupture simulations in ground motion predictions. To do so, we utilize locking models to constrain the stress state and obtain dynamic scenarios and synthetic ground motions for M7 earthquakes in the Nicoya region. By testing different nucleation sites, we quantify the uncertainties in ground motions due to the indeterminism in rupture process. Then we compare our predictions with those from GMMs and scenarios based on two hypothesized homogeneous locking models. Moreover, we check the performance of predictions by comparing them with the observations during the 2012 Nicoya Mw 7.6 earthquake.

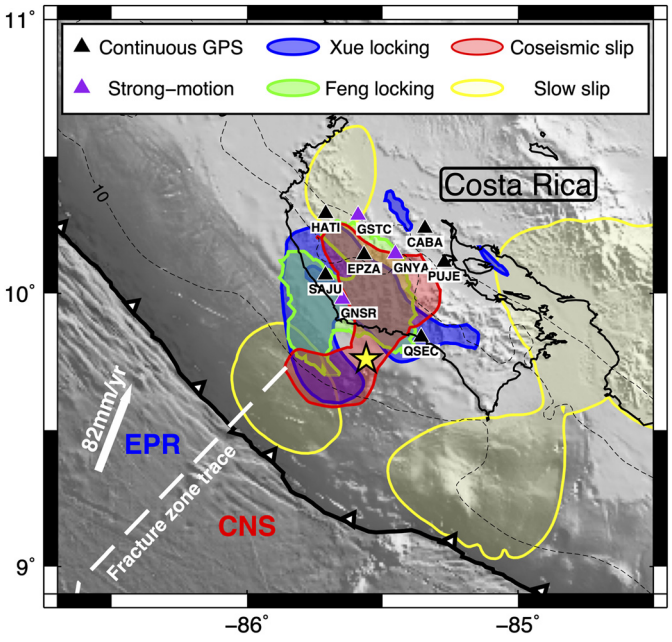

Fig. 1. A map of the Nicoya Peninsula with two interseismic locking models (locking degree > 0.6) (Feng et al., 2012; Xue et al., 2015) and the rupture extent (slip > 1m) of the 2012 Mw 7.6 earthquake (Yue et al., 2013). The yellow star denotes the hypocenter of the 2012 Mw 7.6 event (Yue et al., 2013). Areas with slow slip events are shown in yellow polygons, which represent 1 m of accumulative slip during the interseismic period (Dixon et al., 2014). Triangles indicate the locations of continuous GPS (black) and strong-motion (purple) stations. Dashed lines denote slab top depths of 10 km, 20 km, and 30 km. EPR: East Pacific Rise; CNS: Cocos-Nazca spreading center. (For interpretation of the colors in the figure(s), the reader is referred to the web version of this article.)

2. Method and model setup

2.1. Finite element model setup

We conduct dynamic rupture simulations on a 3-D cuboid elastic model for the Nicoya megathrust, which extends 180 km along strike, 170 km perpendicular to strike, and 80 km at depth. The geographical reference point is at (−85.40, 8.91) and rotated N45°W. We adopt a 2-D curved geometry for the embedded megathrust, the same fault geometry that was used to invert interseismic locking models (Feng et al., 2012; Xue et al., 2015). A 1-D depth-dependent layered velocity model based on the results of seismic receiver function and tomographic images is adopted (Table S1) (Audet and Schwartz, 2013; DeShon et al., 2006).

To meet the numerical requirements to resolve the rupture process, the grid sizes on the fault and the ground surface are set to be 150 m and increase from 150 m near the trench to 3 km on the boundaries. The time step Δt is set as 0.005 s (Madariaga, 1976). The resolution tests in detail can be found in the supplementary file (Fig. S1 & S2). An open-source finite-element package, PyLith, is utilized to solve the dynamic rupture process and ground motions (Aagaard et al., 2013).

2.2. Derive initial stress from the locking models

We estimate initial stress (τ_i) from interseismic locking models following the approach described in Yang et al. (2019a,b) (Fig. 2a & 2d). In Nicoya, the Cocos plate subducts beneath the Caribbean plate with a long-term convergence rate of 82 mm/yr (DeMets et al., 2010), and is characterized by M7.5+ megathrust earthquakes with time intervals of 50 – 60 yrs (Protti et al., 2001). We compute the stress accumulation by assuming a constant slip deficit build-up rate during the interseismic period of 62 yrs, from the last M

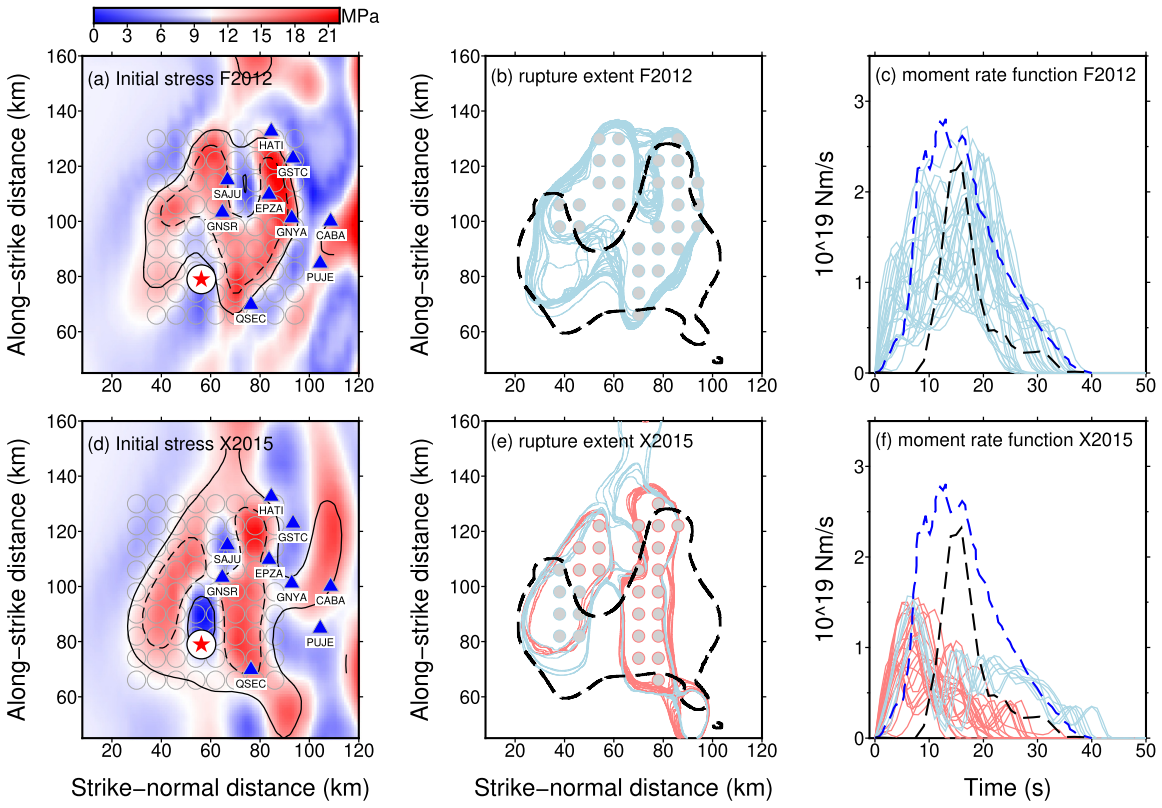

Fig. 2. Dynamic rupture scenarios derived from two locking models. (a) & (d): initial stress patterns derived from models F2012 (a) and X2015 (d). The red stars denote the hypocenter in the 2012 Nicoya Mw 7.6 earthquake (Yue et al., 2013). The blue triangles indicate the locations of GPS and strong-motion stations that provide data to validate predictions. The solid and dashed contours demote areas with locking degrees of 0.5 and 0.75, respectively. (b) & (e): contours for final slip of 1 m in dynamic scenarios (lightblue and lighterd) and in a finite fault model for the 2012 Mw 7.6 event (black dashed, Yue et al., 2013). The circles indicate the nucleation sites that are in the same colors with respective slip contours. (c) & (f): moment rate functions in dynamic scenarios (lightblue and lightred) and from the inversion results for the 2012 Mw 7.6 event (blue: Ye et al., 2013; black: Quintero et al., 2014).

7.5+ event in 1950 to 2012. The linear accumulation assumption is reasonable in Nicoya because the perturbations from other slip events during the interseismic period on the locked megathrust are minor, as discussed in detail in Yang et al. (2019a,b) (Fig. 1). Moreover, the Nicoya megathrust was recently reported to be relocked with a similar locking pattern prior to the 2012 Mw 7.6 event, indicating a relatively stable locking state across earthquake cycles in Nicoya (Xie et al., 2020). The stress calculations are conducted using PyLith. The initial stress (τ_0) is estimated as the summation of the stress accumulation and a constant dynamic stress (τ_d) of 10 MPa. Considering the near-lithostatic pore pressure along the Nicoya megathrust (Audet and Schwartz, 2013; Saffer and Tobin, 2011; Yao and Yang, 2020), we assume a constant effective normal stress (σ_n) of 50 MPa on the fault plane.

There are two locking models for the Nicoya megathrust before the 2012 Nicoya earthquake (Feng et al., 2012; Xue et al., 2015, hereafter termed F2012 and X2015, respectively). Both these models use GPS data from 1996 to 2010, while Xue et al. (2015) add InSAR data from 2007 to 2010 into the inversion, which improves the resolution beneath the Nicoya Peninsula. The total slip deficit rates over the Nicoya megathrust in the two locking models are nearly the same. The onshore locked patches in the two models largely overlap. However, both models suffer from limited resolutions offshore due to the lack of data. The major difference between the two locking models resides in the transition between the onshore and offshore patches. We estimate the initial stress distribution from the two locking models separately.

2.3. Friction law and nucleation

We assume that the megathrust is governed by a linear slip-weakening law (Ida, 1972), which has been widely applied in dynamic rupture simulations. The linear slip-weakening law is characterized by the yield stress (τ_s), the dynamic stress (τ_d), and the critical weakening distance (D_0), over which the strength decreases linearly from τ_s to τ_d. Due to the lack of prior knowledge of frictional properties on faults before the occurrences of earthquakes, we assume that frictional parameters are uniform on the fault. The yield stress (τ_s) on the fault is set to be 20.5 MPa, slightly higher than the maximum of the estimated initial stress, giving a static friction coefficient of ~0.4. The dynamic stress (τ_d) is 10 MPa along the megathrust. The rupture propagation is controlled by the strength excess ($\tau_s - \tau_0$), the strength drop ($\tau_s - \tau_d$), and D_0. In our models, the first two factors are controlled by the interseismic locking model. Therefore, the absolute value of the dynamic stress does not matter. Previous studies have suggested that D_0 should scale with the final slip. However, the final slip in an earthquake is unknown before its occurrence. Moreover, a recent study argues that such scaling may come from the effects of the finite seismogenic width and the fault zone structure (Chen and Yang, 2020). In addition, dynamic simulations suggest that models with a uniform average D_0 or heterogeneous D_0 can result in similar rupture processes and ground motions (Weng and Yang, 2018; Yao and Yang, 2020). Therefore, the critical weakening distance (D_0) is prescribed to be uniform for simplicity (i.e. 0.4 m), a commonly used value in dynamic rupture simulations (e.g. Harris

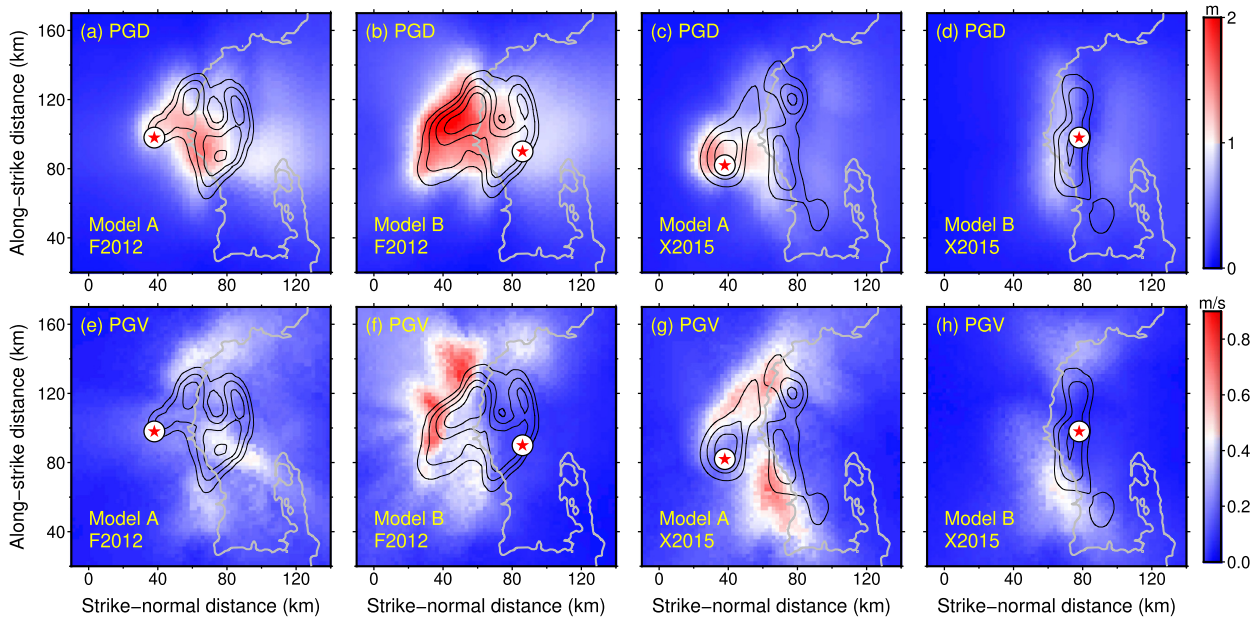

Fig. 3. Ground motion patterns in different dynamic rupture scenarios derived from two locking models. Panels (a) - (d) are PGD distribution and (e) – (h) are PGV patterns. The red stars indicate the hypocenter locations. The black contours are for final slip with intervals of 1 m. The scenarios in (a, b, e, & f) are derived from model F2012, while scenarios in (c, d, g, & h) are derived from model X2015.

et al., 2009). The influence of D_0 on model results will be discussed later in the Discussion section.

We artificially nucleate ruptures by decreasing the yield stress to 0.01 MPa below the initial stress within the nucleation zones (See details in Supplementary file). We consider a radius of 5 km as the upper limit for the nucleation size of M7 earthquakes to minimize artificial effects on the modeled moment magnitudes. By comparing models with 5-km-radius and 3-km-radius nucleation, we find that ruptures with the same nucleation location but different nucleation sizes have nearly identical rupture processes and ground motions (Fig. S3), indicating a minor impact of nucleation size on model results.

3. Dynamic scenarios and ground motions derived from two locking models

We nucleate earthquakes at 72 potential nucleation sites in the locked region and conduct spontaneous rupture simulations based on the initial stress derived from F2012 (Fig. 2a). 29 of the 72 ruptures eventually break the locked region with Mw of 7.5-7.6 (Fig. 2b). Ruptures propagate smoothly over the onshore and offshore patches with rupture speeds of ∼3 km/s (Fig. S4). The rupture extents in these breakaway scenarios are nearly identical with small differences on the offshore patch (Fig. 2b). The rupture durations are 30-40 s, comparable to the duration of the 2012 Mw 7.6 Nicoya earthquake (Fig. 2c) (Ye et al., 2013; Quintero et al., 2014). The maximum slip is 3-4 m (Fig. S4). Besides the 29 cases, other rupture models spontaneously stop before reaching the edges of the locked patch and are almost confined in the nucleation zones, forming self-arresting ruptures with Mw of 5-6.

We follow the same procedure to explore possible rupture scenarios using another locking model (X2015). The low-stress gap between the offshore and onshore patch (Fig. 2d) suppresses the rupture propagation along the dip direction, forming rupture segmentation. Therefore, we obtain 22 ruptures that are confined in the offshore patch or in the onshore patch with Mw of ∼ 7.2 (lightred cluster Fig. 2e). In addition, 7 ruptures initiated offshore (lightblue cluster in Fig. 2e) trigger secondary nucleation on the down-dip high-stress region and eventually break the entire locked zone with Mw of ∼7.5. Due to the low-stress gap, scenarios from X2015 are dominated by along-strike propagation. The rupture durations are ∼40 s and ∼20 s for the Mw∼7.5 and Mw ∼7.2 scenarios respectively (Fig. 2f). The maximum slip in scenarios is also 3-4 m (Fig. S5). In this study, we intend to investigate the potential large earthquakes, therefore self-arresting cases are ignored in the following analyses.

We output the synthetic ground motions (Fig. S6 & S7) and calculate ground motion intensities, including peak ground velocity (PGV), as a standard intensity measure in seismic hazard assessment, and peak ground displacement (PGD) for all dynamic scenarios. PGD is a low-frequency ground motion feature and hence is less affected by the shallow velocity structure. Instead, it is sensitive to low-frequency rupture characteristics such as rupture propagation (Goldberg et al., 2021; Ruhl et al., 2019). Nowadays PGDs are usually measured from the Global Navigation Satellite System (GNSS). Since the displacement signals always diminish quickly in GNSS data for small earthquakes due to the high noise level of several centimeters, the utility of PGD usually focuses on large earthquakes (Goldberg et al., 2021; Ruhl et al., 2019). Considering the large magnitudes (M >7) of our scenarios, we adopt PGD as a ground motion feature here. We do not involve the acceleration predictions in our current study since our synthetics do not cover the frequency band where the energy in ground accelerations concentrates (Fig. S8).

We observe diverse ground motion patterns among models with different rupture directivities or different rupture extents (Fig. 3). For instance, ruptures initiated onshore usually result in higher ground motions (PGD ∼ 2 m; PGV ∼ 0.8 m/s) on the seafloor (Fig. 3b & 3f), nearly twice of those in scenarios nucleated offshore (Fig. 3a & 3e). The directivity effect is not that significant on the Nicoya Peninsula due to the relatively larger distances to the fault plane (Fig. 3a & 3e). In scenarios from X2015, the directivity amplification effect concentrates on the southeast bounds of the locking patches due to the along-strike rupture propagation. In addition, the motions on the seafloor in the onshore segmented scenarios are minor compared to those on the offshore patch (Fig. 3 & S5).

We treat each model equally to generate the distributions of predicted ground motion measures and standard deviations on the ground surface (Fig. 4 and S9). Scenarios from X2015 are divided

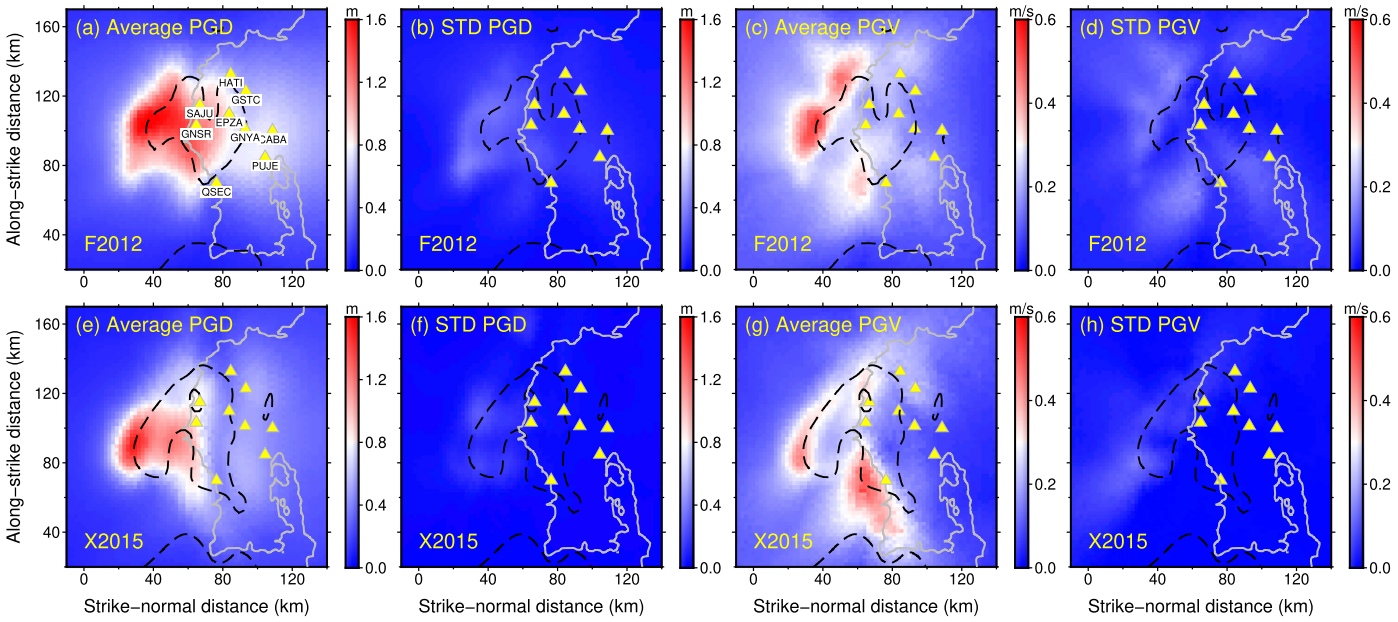

Fig. 4. Synthetic ground motion intensities in Mw ∼7.5 dynamic scenarios from F2012 (a-d) and X2015 (e-h), including the average values and standard deviations for PGD (a, b, e, & f) and PGV (c, d, g, & h). The dashed black contour represents the locking degree of 60%.

into two magnitude bins, one for Mw ∼7.2 and another for Mw ∼7.5. The results indicate higher ground motion intensities offshore compared to the onshore region due to the relatively short hypocentral distance. In Mw∼7.5 scenarios, regions with high PGD overlap with the high-locking regions (Fig. 4a and 4e). The PGDs offshore are comparable in magnitude and pattern in scenarios from the two locking models (Fig. 4a and 4e), while the PGVs show different spatial patterns (Fig. 4c and 4g). The PGV pattern from F2012 smears offshore significantly due to the along-dip rupture directivity (Fig. 4c). The PGV from X2015 for Mw∼7.5 is similar to the locking pattern with slight smearing along strike (Fig. 4g), attributed to the dominant along-strike rupture directivity. The standard deviation is ∼ 30% of the mean values (Fig. 4b, 4d, 4f, & 4h) except the PGD predictions from X2015, in which the standard deviation is <20% due to the relatively consistent rupture process among all scenarios given all hypocenters offshore (Fig. 2e). The predictions from Mw ∼7.2 scenarios are 50% lower compared to Mw ∼ 7.5 scenarios due to the difference in the total moment (Fig. S9). In addition, the standard deviations are larger in Mw 7.2 events due to the diverse rupture extents as shown in Fig. 2e.

4. Comparison with GMMs and kinematic slip deficit models

We compare the dynamic scenarios with two recent GMMs for PGV (Montalva et al., 2021) and PGD (Goldberg et al., 2021), respectively. The PGV model is based on the records in the Chile subduction zone, while the PGD GMM uses a global catalog. In the PGV model, the nearest distance to the rupture plane is used to describe the source-to-site distance (R_{rup}). Here, we define the rupture plane to be the area with slip over 1 m. While in the PGD model, Goldberg et al. (2021) claimed that a weighting function of fault slip can be added to the function to calculate the effective distance to the source (R_{eff}) (eq. (1)).

$$R_{eff} = \left(\sum_{i=1}^{i=n}(w_i R_i^{-4.5})\right)^{-1/4.5} \quad ; \quad w_j = slip_j / \left(\sum_{i=1}^{n} slip_i\right) \qquad (1)$$

where w_i and R_i are the weight and the distance to the site of the i^{th} patch. The w_i is proportional to the slip on the ith subpatch and is normalized to sum to one. In our calculation for R_{eff}, the rupture plane is divided into sub-patches with an interval of 1 km. We keep consistent with GMM models in the calculation of the source-to-site distance, respectively, which results in a slight difference in the source-to-site distance distribution (between R_{rup} and R_{eff}) (Fig. 5).

We sample with intervals of 3 km on the surface to generate the synthetic ground motion datasets from our scenarios. The synthetics generally follow the decay trend of GMMs (Fig. 5). The mean values with standard deviations almost reside in the range predicted by GMMs (Fig. 5). Such consistency reveals the reliability of our scenario predictions. In addition, the PGD and PGV patterns commonly feature higher mean values than GMMs when R_{rup} (R_{eff}) is smaller than 30 km. In addition to the amplitude, the decay rate of PGD in the near field (<30 km) is higher in dynamic scenarios compared to GMMs (Fig. 5). To check the origin of the discrepancies, we calculate the difference between the dynamic-model predictions and the predictions from GMMs (Fig. S10). Since the final slip patterns are generally similar to the slip deficit distribution (Fig. S4 & S5), we adopt the slip deficit models (Fig. 6) to calculate the slip-weight function. To make a fair comparison, we adopt a moment magnitude of 7.5 in GMMs.

The difference between the dynamic models and the GMM predictions reveals the contributions from the source characteristics including the slip distribution on the fault and the rupture directivity (Fig. S10). Compared to the GMM-based predictions, dynamic models produce higher ground motions inside the area where fault slip concentrates and the differences generally decay with R_{rup} (R_{eff}). The difference in PGD becomes nearly zero on average along the contour of 50 km (Fig. S10). Such near-field high values result in the high attenuation rate of PGD with R_{rup} (R_{eff}) in dynamic predictions (Fig. 5). In addition, the difference in PGV is significantly modulated by the rupture directivity effect. The difference may result from the poor representation of the near-field ground motions in GMMs as the available samples within 50 km are very sparse. Such differences in attenuation trend have been observed in large earthquakes such as the 2016 Mw 7.8 Kaikoura earthquake in New Zealand (Bradley et al., 2017) and other physics-based ground motion simulations (Bradley et al., 2017; Bradley, 2019; Xin and Zhang, 2021), which are generally attributed to the local velocity

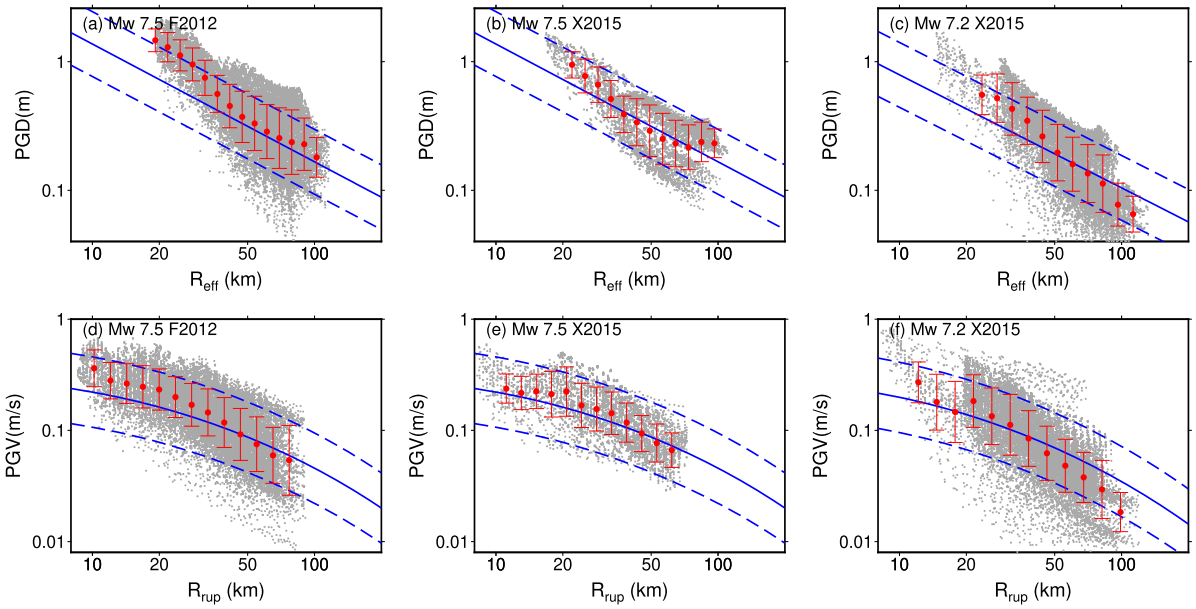

Fig. 5. Synthetic ground motion intensities (gray dots) and ground motion models (GMMs). The synthetics in (a) and (d) are from Mw ~7.5 scenarios from F2012. Synthetics in (b) and (e) are from Mw ~7.5 scenarios from X2015. While synthetics in (c) and (f) are from Mw~7.2 scenarios from X2015. The red dots with error bars indicate the mean values and standard deviations of synthetics. The dashed blue lines indicate the range of GMM predictions with considering standard deviations. The GMMs for PGD and PGV are extracted from Goldberg et al. (2021) and Montalva et al. (2021), respectively.

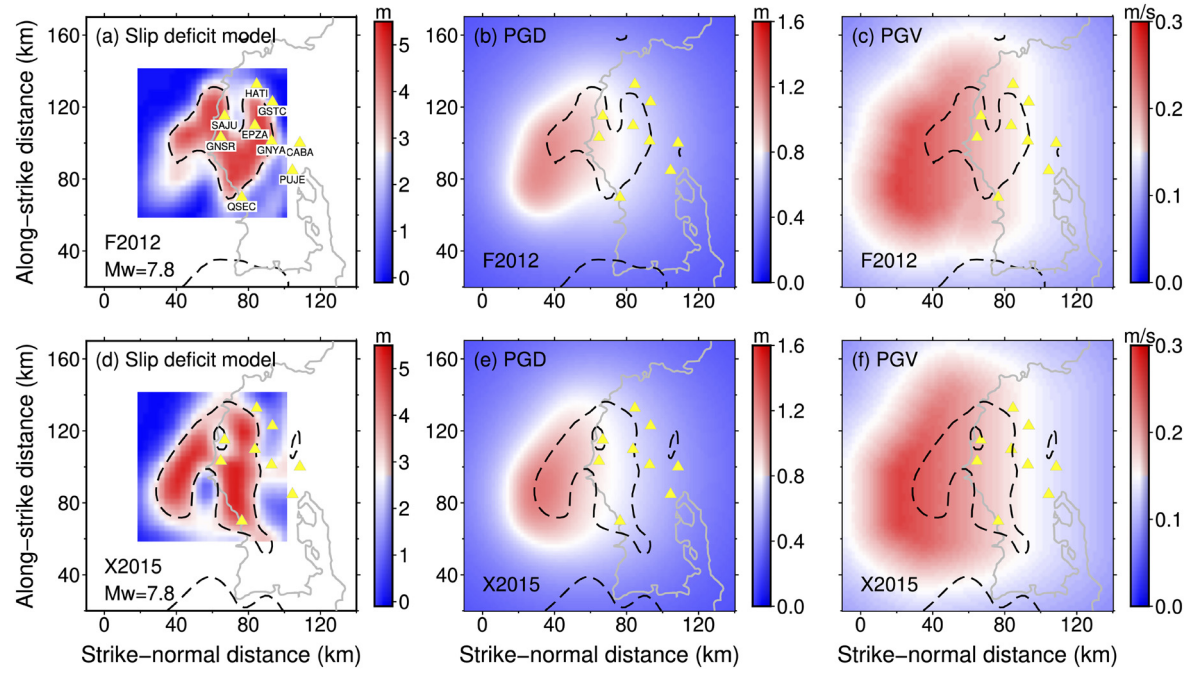

Fig. 6. Kinematic scenarios assuming complete slip deficit release. Panels (a) and (d) are the slip deficit accumulation (62 yrs) in F2012 and X2015, respectively. Panel (b) and (c) are the PGD and PGV predicted based on the scenario in (a) and GMMs (Montalva et al., 2021; Goldberg et al., 2021). Panels (e) and (f) are predictions based on the scenario in panel (d).

structure or the source heterogeneities, including complex fault geometry, heterogeneous slip, and the directivity effect.

We present ground motion predictions using the two GMMs mentioned above and two kinematic models assuming complete slip deficit release as the source models (Fig. 6a & 6d). The final slip in kinematic models is similar to dynamic scenarios but with higher amplitudes (Mw 7.8) (Fig. 6, S4, & S5). Generally, the ground motion patterns (Fig. 6) are spatially smoother compared to dynamic scenarios (Fig. 4). Although with higher moment magnitudes, the kinematic models predict offshore PGDs (Fig. 6b & 6e) slightly smaller than those in dynamic scenarios (Fig. 4a & 4e). Different from the permanent seafloor deformation which is nearly solely determined by the final slip on faults, the PGDs are sensitive to both fault slip and rupture propagation. The higher PGDs in dynamic scenarios reveal the contribution of the rupture process. The PGV predictions from the two kinematic models differ significantly from dynamic scenarios in both amplitude and spatial pattern (Fig. 4 & 6), mainly due to the lack of rupture directivity effect in kinematic scenarios. The peak PGVs in dynamic models are nearly twice those in kinematic models.

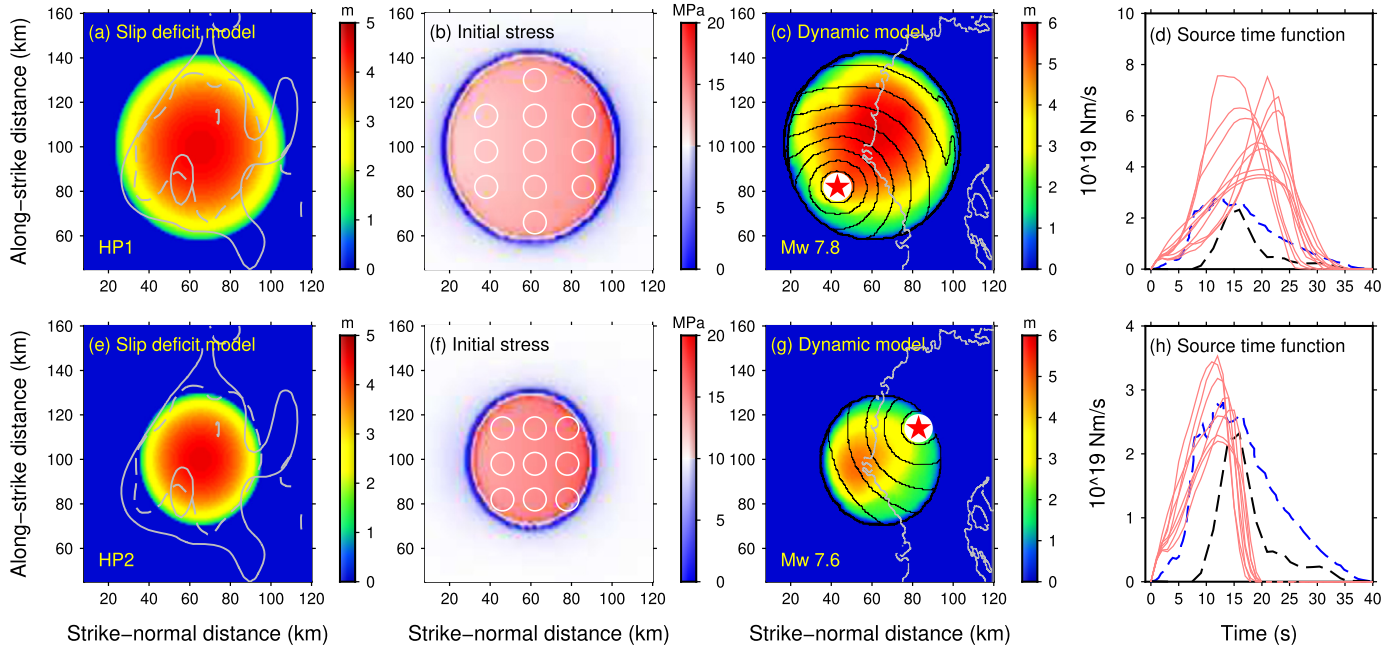

Fig. 7. Scenarios derived from two hypothesized locking models (HP1 and HP2). Panels (a) and (e) represent the accumulated slip deficit (62 yrs) in models HP1 and HP2, respectively. Panels (b) and (f) denote the stress accumulation in the two models. The white circles represent the tested hypocenter locations. Panels (c) and (g) show final slip in two scenarios. The black contours are rupture fronts of every 3 s. Panels (d) and (h) show the moment rate functions in dynamic scenarios, compared with inversion results for the 2012 Nicoya Mw 7.6 earthquake (blue: Ye et al., 2013; black: Quintero et al., 2014).

5. Scenarios derived from homogenous stress distribution

To further illustrate the impact of stress heterogeneity, we test extreme cases under homogeneous stress conditions. First, we assume a circular locking patch (Fig. 7a), where the locking degree is 1 at the center and gradually decreases with the distance from the center (eq. (2)):

$$D(r) = D_0\sqrt{1-\left(\frac{r}{R}\right)^2} \tag{2}$$

where D is the slip deficit, as a function of the distance from the center (r); D_0 is the slip deficit at the center; and R is the radius of the patch (i.e. 40 km). The stress pattern is smooth inside the patch (Fig. 7b). Due to the moderate stress level, ruptures nucleated by decreasing the yield stress to 0.01 MPa lower than the initial stress mostly become self-arresting. Therefore, we change the nucleation strategy by increasing the initial stress to a level of 0.1 MPa higher than the yield stress. We first set the total slip deficit to be equal to the total amount in the major locking zone in the two interseismic locking models. This hypothesized locking model is termed HP1 hereafter. The moment magnitudes of dynamic rupture scenarios from HP1 are ~7.8 (Fig. 7c), close to the value estimated by assuming a complete slip deficit release. The durations of ruptures are ~30-35 s (Fig. 7d). We further decrease the slip deficit by 60% inside the homogeneous patch (hereafter termed as locking model HP2) (Fig. 7e & 7f) and yield Mw 7.53 ~ 7.61 scenarios with durations ~20 s (Fig. 7g & 7h). The average rupture speeds in those scenarios are ~3-3.5 km/s.

We follow the same procedure to generate ground motion predictions from both dynamic and kinematic scenarios (through GMMs) for HP1 and HP2, respectively. The ground motion amplitudes in kinematic models are proportional to the total slip deficit as indicated by the comparison between HP1 and HP2 models (Fig. 8). Given the same total slip deficit, the kinematic models, including X2015, F2012, and HP1, result in similar predictions in both amplitude and spatial extent (Fig. 6 and Fig. 8). Differently, the ground motions in dynamic scenarios under the homogeneous condition (HP1) are much severer compared to those in heterogeneous models (X2015 and F2012) (Fig. 4). The peak PGD is ~4 m in dynamic scenarios from HP1 (Fig. 8a), much higher than the dynamic predictions from X2015 and F2012 (i.e. ~1.6 m, Fig. 4). Similar amplification has been observed in PGV offshore (Fig. 8b).

Given similar rupture extent and moment magnitude among dynamic scenarios from F2012, X2015, and HP2, the ground motions in HP2 scenarios are more intense than X2015 and F2012 with peak PGD and PGV of 2.5 m and 0.7 m/s, respectively (Fig. 8e and 8f). The major cause is the faster moment release in homogeneous models. The rupture fronts expand as nearly circles in homogeneous models (Fig. 7). While the rupture fronts are confined and reshaped by the stress heterogeneities in X2015 and F2012 models (Fig. S4 & S5). Consequently, dynamic models from HP2 (Fig. 7h) feature higher peak moment rates and shorter durations compared to X2015 and F2012 (Fig. 2), which enhances near-field ground motions.

6. Compare predictions with observations during the 2012 Mw7.6 earthquake

We compare the ground motion predictions with observations during the 2012 Nicoya Mw 7.6 earthquake. We collect data on 6 high-rate GPS stations (5 Hz) and 3 strong-motion stations (200 Hz) with R_{rup} (R_{eff}) of 20-60 km. PGVs are picked in the frequency band of < 0.5 Hz. PGDs are compared at 6 high-rate GPS stations without any filter. The 3 strong-motion stations are excluded in the PGD validation due to the baseline shift in converting acceleration into displacement (Fig. S11 & S12). The displacement obtained by double integration of the ground acceleration data often shows large drift, for reasons that include the ground tilt, inelastic ground deformation, and hysteresis in the instruments (Bock et al., 2011). The PGDs and PGVs reside in the ranges of 0.4-0.8 m and 0.10-0.25 m/s, respectively.

We first introduce the predictions with standard deviations based on dynamic scenarios from X2015 and F2012 for PGV and

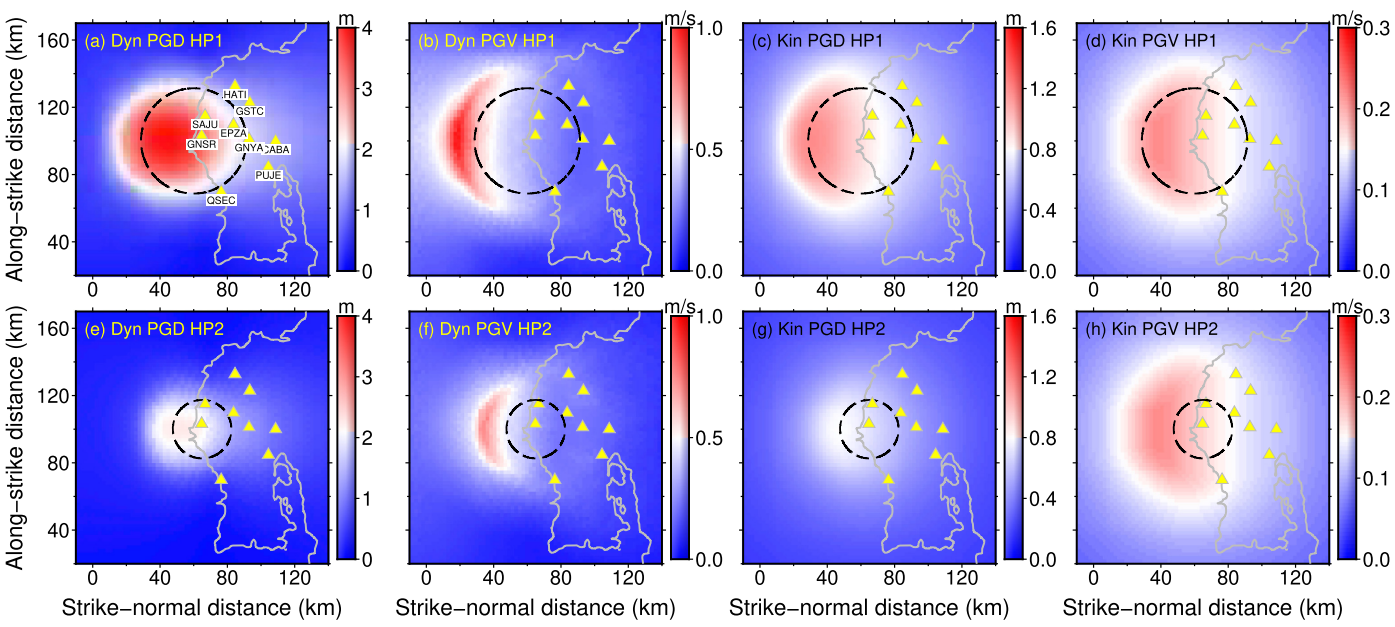

Fig. 8. Ground motion predictions based on the models HP1 and HP2. The predictions from dynamic scenarios are plotted in panels (a, b, e, and f). The predictions through GMMs using kinematic models assuming complete slip deficit release are plotted in panels (c, d, g, and h).

PGD on each station (Fig. 9). Most individual PGV measures and half of PGD measures are captured with errors smaller than one standard deviation in predictions from F2012 (Fig. 9a & 9b). Predictions from X2015 largely underpredict the ground motions on three landward stations: GNYA, PUJE, and CABA. The underpredictions can be attributed to the shallow down-dip bounds compared to the 2012 Mw 7.6 earthquake (Fig. 2e). In addition, the 2012 Mw 7.6 earthquake propagated towards down-dip, while the downward propagation is largely slowed down by the low-stress gap in scenarios from X2015. In addition, the rupture patches are more elongated along the strike direction in scenarios from X2015, which enhances the rupture directivity effects along strike, leading to overpredictions on stations SAJU, QSEC, and HATI. The predictions from the F2012 do a better job of capturing the observations, mostly due to the larger overlap in rupture extent with the 2012 Mw 7.6 event (Fig. 2b) and the smooth rupture propagation along the dip direction. Besides, the dynamic scenarios from HP1 and HP2 generally overpredict ground motions, especially in PGD (Fig. 9c & 9d). The average PGD prediction is ∼2-3 times of observations. In addition, we generate predictions from the two GMMs by using a finite fault slip model for the 2012 Mw 7.6 earthquake (Yue et al., 2013) as the source model (Fig. 9 a-d). The GMM-based predictions capture all data within one standard deviation and overall fit observed PGDs (Fig. 9a). However, they underpredict the PGV amplitudes (Fig. 9a & 9b). Noted that the standard deviations in GMMs are obviously larger than the scenario predictions.

To quantify the errors, we define the residual as the natural log of the ratio between the observation and the prediction (Fig. 9e & 9f). The average of the absolute residuals (|ln(data/predictions)|) for PGD for dynamic predictions in X2015, F2012, HY1, HY2, and the GMM are 0.18, 0.33, 1.11, 0.58, and 0.22, respectively. The average residuals for PGV are 0.47, 0.17, 0.32, 0.29, and 0.72, respectively. Note that the predictions from the GMM feature good performance in PGD predictions partly because we use the source model in Yue et al. (2013) for the 2012 Mw 7.6 earthquake that was constrained from observations. However, the slip distribution before an earthquake is unknown and thus it is unfair to conclude a superior performance of GMM. Dynamic scenarios from X2015 provide comparable performance in predicting PGDs. Overall, the scenarios from F2012 provide the best fitting on the PGV measurements. The GMM largely underpredicts PGVs. However, comparison in PGV may bear uncertainties due to the lack of detailed information of the shallow structure.

We further calculate the spectra for synthetic and observed velocity waveforms (Fig. S13-S18). The spectra of data indicate that the energy of the ground velocity during the 2012 Mw 7.6 earthquake concentrates in the frequency band of 0.02–0.2 Hz. Predictions in scenarios from F2012 capture more characteristics of the shape and the amplitude of observations (Fig. S13 & S14). The predicted velocity spectra from F2012 exhibit remarkable consistency with data in the frequency band of 0.05–0.5 Hz for most stations and drop drastically over 0.5 Hz (Fig. S13 & S14). The high-frequency energy (>0.5 Hz) is largely underpredicted in the horizontal components, which is the reason to apply a lowpass filter of 0.5 Hz before picking PGVs. While the underprediction is minor in the vertical component. This may be attributed to the more complex S-wave velocity structure than the P-wave velocity structure. As detailed shallow structure is lacking in our models, we adopt the reference velocity V_{S30} (i.e. 0.75 km/s) in the PGV GMM. Although such simplification potentially leads to bias when comparing with GMMs in PGV amplitude, the trend of decay should be similar. The amplitudes of velocity spectra in low frequency represent the coseismic static offsets which are mostly determined by the final slip distribution on fault. Therefore, the discrepancies in the low-frequency limit are attributed to the differences in the final slip between scenarios and the 2012 Mw 7.6 event (Fig. 2b).

7. Discussion

7.1. Potential contribution to seismic hazard analysis

One potential contribution from the dynamic scenarios is the prediction of rupture directivity and ground motion spatial patterns. Our model results suggest that the spatial patterns largely depend on the location of the slip patch and the rupture directivity. The locking models can help identify the location and the spatial extent of asperities. Rupture dynamic simulation can contribute by identifying potential rupture directivity given the initial stress condition on faults. Besides the stress condition, other

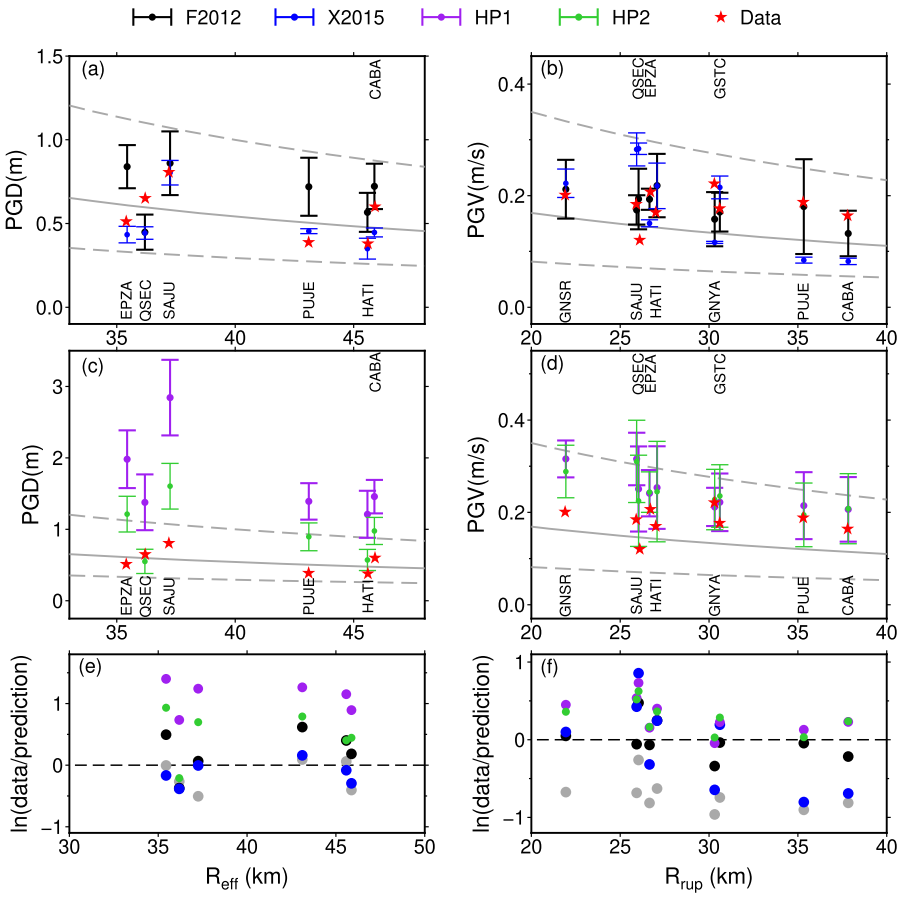

Fig. 9. Predictions and residuals of PGD (a, c, & e) and PGV (b, d, & f) on near-field GPS and strong-motion stations. The predictions from dynamic rupture scenarios based on the locking models F2012, X2015 (Mw ~7.5 scenarios), HP1, and HP2 are plotted in black, blue, purple, and green, respectively. The red stars are observations during the 2012 Mw 7.6 earthquake. The gray solid and dash lines are predictions with standard deviations from PGD (Goldberg et al., 2021) and PGV (Montalva et al., 2021) GMMs by using a finite fault slip model (Yue et al., 2013) as the source. The panel (e) and (f) show the residuals of the individual prediction colored respectively.

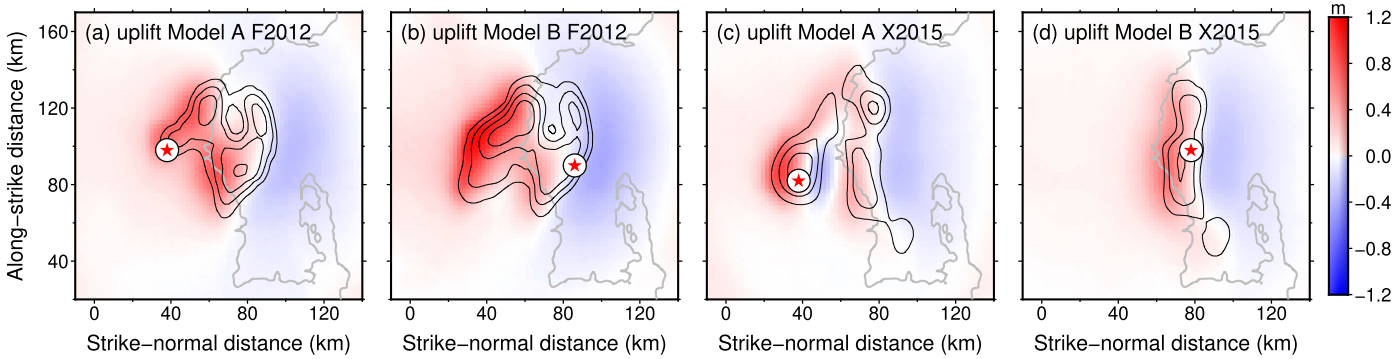

Fig. 10. Coseismic vertical deformation in dynamic rupture scenarios. Positive values stand for surface uplift. The red stars indicate the hypocenter locations. The black contours represent fault slip with intervals of 1 m.

factors that impact rupture directivity such as material contrast across faults (Andrews and Ben-Zion, 1997), variation in seismogenic depth (Chen, 2021), and shallow low-velocity zones (Weng et al., 2016) can also be included in dynamic modeling. Although there have been studies on directivity rectification in GMMs (Spudich and Chiou, 2008; Spudich et al., 2014), which usually assume the amplification factor to decay with hypocentral distance or increase with the rupture extent, those explicit functions might still be too basic to capture ground motion characteristics, especially in the near field for large earthquakes with high complexities (Xin and Zhang, 2021). In addition to the ground motions, the coseismic seafloor uplift is important in subduction zone regions as it determines the tsunami potential. Similar to the ground motion patterns, the seafloor uplift pattern in our scenarios also varies with hypocenter location and locking model (Fig. 10). The synthetic seafloor deformation can be further applied as input for tsunami modeling.

Besides dynamic scenarios, there have been other efforts to involve the constraints from interseismic geodetic data or locking models to constrain the source models in ground motion predictions and further hazard analysis. Usually, geodetic data are used to constrain kinematic behaviors on faults, e.g. the fault slip. For instance, the surface velocity fields have been applied to constrain the long-term slip rates (moment budgets) of particular faults or

over a spatially distributed region in generating seismicity rate models (Field et al., 2017). Moreover, a recent study proposed a new method to utilize locking models as prior information in earthquake stochastic modeling and probabilistic tsunami hazard assessment for the Cascadia subduction zone (Small and Melgar, 2021; Melgar et al., 2022). As we mentioned in the introduction, the slip deficit is not a mirror image of coseismic slip considering the uncertainties in estimating slip deficit. Our models further suggest that the coseismic slip can be only ∼40% of the accumulated slip deficit due to the incomplete stress release, especially near the boundaries of asperities. Such discrepancy is also observed in dynamic scenarios for the Anninghe fault (Yao and Yang, 2022) and the energy-based scenarios for the Nankai trough (Noda et al., 2021). The fraction of coseismic slip to slip deficit negatively correlates with stress roughness. This study, as well as other studies on locking-based scenarios, can provide references for coseismic slip in source modeling in seismic hazard assessment.

Currently, ground motion predictions are dominantly conveyed through GMMs, which are proven to be effective and have been widely applied for engineering use. Although some recent studies have suggested that the PBSs are more effective in solving ground motions in cases with complex sources such as multi-segment ruptures (Bradley et al., 2017; Xin and Zhang, 2021), the application of PBSs still faces many challenges such as how to explicitly quantify the uncertainties (Bradley, 2019). Our simulations suggest a standard deviation of ∼ 30% purely due to the rupture indeterminism (Fig. 4), which should be considered an important source of uncertainty.

7.2. Uncertainties from assumptions and further improvement

Our modeling results indicate that rupture extent, rupture directivity, and surface response in earthquakes are highly dependent on the stress pattern, underlining the importance of considering stress heterogeneity in source modeling. The stress patterns derived from locking models are sensitive to the spatial gradient of the locking degree. Therefore, a precise locking distribution is critical. However, due to the lack of offshore geodetic observations, locking models for megathrusts usually suffer from low resolutions, especially for the portions near trenches (Li et al., 2018). In Nicoya, the station coverage is excellent among subduction zones because the Nicoya Peninsula protrudes seaward and the distance from the coast to the trench is only ∼40 km. The locking models in Nicoya capture the heterogeneities in the scale of 10-20 km (Feng et al., 2012; Xue et al., 2015). The lack of resolution in smaller scales limits the frequency of ground motions derived from locking models. Therefore, we expect a better performance of this approach with good geodetic data coverage, which can capture smaller-scale heterogeneities.

In addition, the assumption of a linear stress accumulation during the interseismic period may lead to uncertainties in estimating the initial stress. Geodetic observations and numerical models suggest that the locking state on faults can evolve with time (Bruhat and Segall, 2017; Noda and Lapusta, 2013). Although the assumption seems to be reasonable for the Nicoya case as discussed in session 2.2, it needs to be considered carefully for other regions. Moreover, we assume uniform background stress and ignore the contribution of previous seismicity on the stress pattern. Although ruptures to some degree can smooth the stress mostly inside the rupture area, they additionally introduce stress concentration near the rupture bounds, as another important source of stress heterogeneities. Dynamic simulations suggest that such heterogeneities introduced by previous seismicity can modulate rupture propagation. The consequent abrupt changes in rupture speed when encountering barriers or asperities can largely enhance the high-frequency radiation and the ground motion (Oral et al., 2022; Madariaga, 1983). Moreover, with the nonuniform residual stress, the stress pattern evolves and can result in various rupture extents and magnitudes over earthquake cycles (Kaneko et al., 2010; Yang et al., 2012b; Luo and Ampuero, 2018; Noda and Lapusta, 2013), forming super-cycle behaviors. It is our future work to involve such long-term factors.

In our models, we simply assume the D_0 to be 0.4 m. This value resides in the range constrained by dynamic inversion for the 2012 Nicoya Mw 7.6 earthquake on the major down-dip slip patch (Yao and Yang, 2020). However, the estimates from observations for D_0 bear considerable uncertainties due to the intrinsic trade-off with strength drop (Guatteri and Spudich, 2000). Here we provide a synthetic test on the sensitivity of our models to D_0. Models with different D_0 values (i.e., 0.6 m and 0.8 m) are conducted (Fig. S19). The comparison indicates that increasing D_0 can obviously slow down the rupture. The decrease in rupture speed weakens the directivity effect and PGV, although the patterns remain similar. In comparison, there is no obvious change in the final slip distribution. The change in PGD is also minor as it represents a lower-frequency feature compared to PGV. The dependence of scenarios on D_0 highlights the necessity of incorporating independent constraints on frictional parameters in future work.

Besides the initial stress, other model inputs of off-fault structures and material properties also play critical roles in controlling the rupture process (Dunham, 2007; Weng and Yang, 2018). Our approach can be further developed by involving more heterogeneities. For instance, we have ignored variations in frictional properties on faults in models, making the ruptures confined in the locked region (Fig. 2). However, ruptures may extend outside the locked regions and break aseismic portions, depending on the contrast in frictional properties between locked and aseismic regions (Kaneko et al., 2010; Ramos and Huang, 2019). In addition, material properties, especially the seismic velocity and anelastic attenuation, along the source-to-site paths can also largely influence ground motion amplitudes and have been considered in ground motion models (GMM) in regional-specific probabilistic seismic hazard assessment (PSHA) either via the values of the material properties themselves (Sahakian et al., 2019) or empirically based spatially varying coefficients (Lanzano et al., 2021; Sgobba et al., 2021). To improve the synthetic ground motions, especially in high frequencies, finer material properties with detailed shallow sediment structures should be incorporated (Olsen, 2000; Pitilakis et al., 2013).

8. Conclusion

We obtain rupture scenarios and synthetic ground motions through dynamic rupture simulations with constraints from two interseismic locking models in the Nicoya Peninsula (X2015 and F2012). The synthetic ground motions are generally consistent with GMMs in attenuation trend. We further generate synthetic ground motion patterns using the kinematic slip deficit models and GMMs. However, the spatial patterns in dynamic scenarios differ a lot from those in kinematic scenarios. Such differences are mainly attributed to the rupture directivity effects. In addition, we test models with homogeneous stress conditions. The results indicate that the stress heterogeneities tend to cause incomplete stress release and therefore smaller earthquake magnitudes. Moreover, we observe different rupture directivity in scenarios from different locking models, revealing the dependency of rupture directivity on the stress pattern. Furthermore, the predictions from F2012 show great consistency with the observations during the 2012 Mw 7.6 Nicoya earthquakes. Our results highlight the importance of involving stress heterogeneities in dynamic scenarios and the potential contribution of locking models in source modeling for seismic hazard assessment.

CRediT authorship contribution statement

Both authors contributed in developing main ideas, interpreting the results, and producing the manuscript.

Declaration of competing interest

The authors declare that they have no known competing financial interests or personal relationships that could have appeared to influence the work reported in this paper.

Data availability

The data used in this study are all open-access.

In this study, we utilize ground motion recordings at 6 high-rate GPS (sampling rate: 5 /s) and 3 strong motion stations (sampling rate: 200 /s) for the 2012 Mw 7.6 earthquake. The time series of GPS data can be downloaded from UNAVCO https://www.unavco.org/data/gps-gnss/gps-gnss.html. The strong motion data can be downloaded from LIS-UCR http://www.lis.ucr.ac.cr. We obtain three-component ground displacement data of the high-rate GPS from Yin and Wdowinski (2014). The displacement series of GPS data are further transformed into velocity waveforms and acceleration waveforms. We integral the acceleration data on strong-motion stations into velocity waveforms.

Acknowledgements

This study is supported by Hong Kong Research Grant Council Grants (14306418, 14306119), CUHK Direct Grant from Faculty of Science, China Earthquake Science Experiment Project, CEA (2018CSES0102), The Open Foundation of the United Laboratory of Numerical Earthquake Forecasting (grant No. 2021LNEF02).

Appendix A. Supplementary material

Supplementary material related to this article can be found online at https://doi.org/10.1016/j.epsl.2022.117905.

References

Aagaard, B.T., Knepley, M.G., Williams, C.A., 2013. A domain decomposition approach to implementing fault slip in finite-element models of quasi-static and dynamic crustal deformation. J. Geophys. Res. 118, 3059–3079.

Ader, T., Avouac, J.-P., Liu-Zeng, J., Lyon-Caen, H., Bollinger, L., Galetzka, J., et al., 2012. Convergence rate across the Nepal Himalaya and interseismic coupling on the Main Himalayan Thrust: implications for seismic hazard. J. Geophys. Res. 117, B04403. https://doi.org/10.1029/2011JB009071.

Andrews, D.J., Ben-Zion, Y., 1997. Wrinkle-like slip pulse on a fault between different materials. J. Geophys. Res. 102 (B1), 553–571. https://doi.org/10.1029/96JB02856.

Atkinson, G., Boore, D., 1995. New ground motion relations for eastern North America. Bull. Seismol. Soc. Am. 85, 17–30.

Audet, P., Schwartz, S.Y., 2013. Hydrologic control of forearc strength and seismicity in the Costa Rican subduction zone. Nat. Geosci. 6 (10), 852–855.

Avouac, J., Meng, L., Wei, S., et al., 2015. Lower edge of locked Main Himalayan Thrust unzipped by the 2015 Gorkha earthquake. Nat. Geosci. 8, 708–711. https://doi.org/10.1038/ngeo2518.

Baranes, H., Woodruff, J.D., Loveless, J.P., Hyodo, M., 2018. Interseismic coupling-based 460 earthquake and tsunami scenarios for the Nankai Trough. Geophys. Res. Lett. 461 (45), 2986–2994. https://doi.org/10.1002/2018GL077329.

Bindi, D., Pacor, F., Luzi, L., Puglia, R., Massa, M., Ameri, G., Paolucci, R., 2011. Ground motion prediction equations derived from the Italian strong motion database. Bull. Seismol. Soc. Am. Eng 9, 1899. https://doi.org/10.1007/s10518-011-9313-z.

Bock, Y., Melgar, D., Crowell, B.W., 2011. Real-time strong-motion broadband displacements from collocated GPS and accelerometers. Bull. Seismol. Soc. Am. 101 (6), 2904–2925.

Boore, D., Atkinson, G., 2008. Ground-motion prediction equations for the average horizontal component of PGA, PGV, and 5%-damped PSA at spectral periods between 0.1 s and 10.0 s. Earthq. Spectra 24 (1), 99–138.

Bradley, B.A., 2019. On-going challenges in physics-based ground motion prediction and insights from the 2010–2011 Canterbury and 2016 Kaikoura, New Zealand earthquakes. Soil Dyn. Earthq. Eng. 124, 354–364.

Bradley, B.A., Razafindrakoto, H.N.T., Polak, V., 2017. Groundmotion observations from the 14 November 2016 Mw 7.8 Kaikoura, New Zealand, earthquake and insights from broadband simulations. Seismol. Res. Lett. 88, 740–756.

Bruhat, L., Segall, P., 2017. Deformation rates in northern Cascadia consistent with slow updip propagation of deep interseismic creep. Geophys. J. Int. 211, 427–449. https://doi.org/10.1093/gji/ggx317.

Bydlon, S.A., Withers, K.B., Dunham, E.M., 2019. Combining dynamic rupture simulations with ground-motion data to characterize seismic hazard from Mw 3 to 5.8 earthquakes in Oklahoma and Kansas. Bull. Seismol. Soc. Am. 109 (2), 652–671. https://doi.org/10.1785/0120180042.

Chen, X., 2021. Investigations of Fault Friction Parameters and Rupture Characteristics on Finite Seismogenic Faults. The Chinese University of Hong, Kong.

Chen, X., Yang, H., 2020. Effects of seismogenic width and low-velocity zones on estimating slip-weakening distance from near-fault ground deformation. Geophys. J. Int. 223 (3), 1497–1510. https://doi.org/10.1093/gji/ggaa385.

Chlieh, M., Perfettini, H., Tavera, H., Avouac, J.-P., Remy, D., Nocquet, J.-M., et al., 2011. Interseismic coupling and seismic potential along the Central Andes subduction zone. J. Geophys. Res. 116, B12405. https://doi.org/10.1029/2010JB008166.

DeMets, C., Gordon, R.G., Argus, D.F., 2010. Geologically current plate motions. Geophys. J. Int. 181 (1), 1–80.

DeShon, H.R., Schwartz, S.Y., Newman, A.V., Gonzalez, V., Protti, M., Dorman, L.R.M., et al., 2006. Seismogenic zone structure beneath the Nicoya Peninsula, Costa Rica, from three-dimensional local earthquake P- and S-wave tomography. Geophys. J. Int. 164 (1), 109–124.

Dixon, T.H., Jiang, Y., Malservisi, R., McCaffrey, R., Voss, N., Protti, M., Gonzalez, V., 2014. Earthquake and tsunami forecasts: relation of slow slip events to subsequent earthquake rupture. Proc. Natl. Acad. Sci. USA 111 (48), 17039–17044.

Dunham, E.M., 2007. Conditions governing the occurrence of supershear ruptures under slip-weakening friction. J. Geophys. Res. 112, B07302. https://doi.org/10.1029/2006JB004717.

Feng, L., Newman, A.V., Protti, M., Gonzalez, V., Jiang, Y., Dixon, T.H., 2012. Active deformation near the Nicoya Peninsula, northwestern Costa Rica, between 1996 and 2010: interseismic megathrust coupling. J. Geophys. Res., Solid Earth 117, B06407.

Field, E.H., Jordan, T.H., Page, M.T., Milner, K.R., Shaw, B.E., Dawson, T.E., et al., 2017. A synoptic view of the third Uniform California Earthquake Rupture Forecast (UCERF3). Seismol. Res. Lett. 88 (5), 1259–1267. https://doi.org/10.1785/0220170045.

Chan, Y.P.B., Yao, S., Yang, H., Wang, K., 2022. Estimation of rupture scenarios along the Cascadia megathrust from interseismic locking models. In: EGU Meeting 2022. EGU22-12624.

Goldberg, D.E., Melgar, D., Hayes, G.P., Crowell, B.W., Sahakian, V.J., 2021. A ground-motion model for GNSS peak ground displacement. Bull. Seismol. Soc. Am. 111 (5), 2393–2407.

Guatteri, M., Spudich, P., 2000. What can strong-motion data tell us about slip-weakening fault-friction laws? Bull. Seismol. Soc. Am. 90 (1), 98–116. https://doi.org/10.1785/0119990053.

Harris, R.A., et al., 2009. The SCEC/USGS dynamic earthquake rupture code verification exercise. Seismol. Res. Lett. 80 (1), 119–126. https://doi.org/10.1785/gssrl.80.1.119.

Harris, R.A., 2004. Numerical simulations of larger earthquakes: dynamic rupture propagation on heterogeneous faults. In: Donnellan, A., Mora, P., Matsu'ura, M., Yin, X. (Eds.), Computational Earthquake Science Part II. PAGEOPH Topical Volumes. Birkhäuser, Basel.

Hok, S., Fukuyama, E., Hashimoto, C., 2011. Dynamic rupture scenarios of anticipated Nankai-Tonankai earthquakes, southwest Japan. J. Geophys. Res. 116, B12319. https://doi.org/10.1029/2011JB008492.

Ida, Y., 1972. Cohesive force across the tip of a longitudinal-shear crack and Griffith's specific surface energy. J. Geophys. Res. 77 (20), 3796–3805.

Kaneko, Y., Avouac, J.-P., Lapusta, N., 2010. Towards inferring earthquake patterns from geodetic observations of interseismic coupling. Nat. Geosci. 3, 363–369.

Lanzano, G., Sgobba, S., Caramenti, L., Menafoglio, A., 2021. Ground-MotionModel for crustal events in Italy by applying the multisource geographically weighted regression (MSGWR) method. Bull. Seismol. Soc. Am. 111 (6), 3297–3313.

Li, S., Wang, K., Wang, Y., Jiang, Y., Dosso, S.E., 2018. Geodetically inferred locking state of the Cascadia megathrust based on a viscoelastic Earth model. J. Geophys. Res., Solid Earth 123, 8056–8072. https://doi.org/10.1029/2018JB015620.

Luo, Y., Ampuero, J.P., 2018. Stability of faults with heterogeneous friction properties and effective normal stress. Tectonophysics (ISSN 0040-1951) 733, 257–272. https://doi.org/10.1016/j.tecto.2017.11.006.

Madariaga, R., 1983. High frequency radiation from dynamic earthquake. Ann. Geophys. 1, 17–23.

Madariaga, R., 1976. Dynamics of an expanding circular fault. Bull. Seismol. Soc. Am. 66 (3), 639–666.

Melgar, D., Sahakian, V.J., Thomas, A.M., 2022. Deep coseismic slip in the Cascadia megathrust can be consistent with coastal subsidence. Geophys. Res. Lett., e2021GL097404.

Métois, M., Socquet, A., Vigny, C., Carrizo, D., Peyrat, S., Delorme, A., Maureira, E., Valderas-Bermejo, M.-C., Ortega, I., 2013. Revisiting the North Chile seismic gap segmentation using GPS-derived interseismic coupling. Geophys. J. Int. 194 (3), 1283–1294. https://doi.org/10.1093/gji/ggt183.

Montalva, M.A., Bastías, Nicolás, Leyton, Felipe, 2021. Strong ground motion prediction model for PGV and spectral velocity for the Chilean subduction zone. Bull. Seismol. Soc. Am. 112 (1), 348–360. https://doi.org/10.1785/0120210037.

Moreno, M., Rosenau, M., Oncken, O., 2010. 2010 Maule earthquake slip correlates with pre-seismic locking of Andean subduction zone. Nature 467 (7312), 198–202.

Noda, A., Saito, T., Fukuyama, E., Urata, Y., 2021. Energy-based scenarios for great thrust-type earthquakes in the Nankai trough subduction zone, southwest Japan, using an interseismic slip-deficit model. J. Geophys. Res., Solid Earth 126, e2020JB020417. https://doi.org/10.1029/2020JB020417.

Noda, H., Lapusta, N., 2013. Stable creeping fault segments can become destructive as a result of dynamic weakening. Nature 493, 518–521. https://doi.org/10.1038/nature11703.

Olsen, K.B., 2000. Site amplification in the Los Angeles basin from three-dimensional modeling of ground motion. Bull. Seismol. Soc. Am. 90 (6B), S77–S94. https://doi.org/10.1785/0120000506.

Olsen, K.B., Day, S.M., Minster, J.B., Cui, Y., Chourasia, A., Faerman, M., Moore, R., Maechling, P., Jordan, T.H., 2006. Strong shaking in Los Angeles expected from southern San Andreas earthquake. Geophys. Res. Lett. 33, L07305. https://doi.org/10.1029/2002JB002235.

Oral, E., Ampuero, J.P., Ruiz, J., Asimaki, D., 2022. A method to generate initial fault stresses for physics-based ground motion prediction consistent with regional seismicity. https://resolver.caltech.edu/CaltechAUTHORS:20220520-388187000. Unpublished.

Perfettini, H., Avouac, J.-P., Tavera, H., Kositsky, A., Nocquet, J.-M., Bondoux, F., Chlieh, M., Sladen, A., Audin, L., Farber, D.L., Soler, P., 2010. Seismic and aseismic slip on the Central Peru megathrust. Nature 456, 78–81. https://doi.org/10.1038/nature09062.

Pitilakis, K., Riga, E., Anastasiadis, A., 2013. New code site classification, amplification factors and normalized response spectra based on a worldwide ground-motion database. Bull. Earthq. Eng. 11, 925–966. https://doi.org/10.1007/s10518-013-9429-4.

Protti, M., González, V., Newman, A.V., Dixon, T.H., Schwartz, S.Y., Marshall, J.S., Feng, L., Walter, J.I., Malservisi, R., Owen, S.E., 2014. Nicoya earthquake rupture anticipated by geodetic measurement of the locked plate interface. Nat. Geosci. 7, 117–121.

Protti, M., Güendel, F., Malavassi, E., 2001. Evaluación del potencialsísmico de laPenínsula de Nicoya, Heredia Costa Rica. Editorial Fundación UNA. 144 p.

Quintero, R., Zahradník, J., Sokos, E., 2014. Near-regional CMT and multiple-point source solution of the September 5, 2012, Nicoya, Costa Rica Mw 7.6 (GCMT) earthquake. J. South Am. Earth Sci. 55, 155–165.

Ramos, M.D., Huang, Y., 2019. How the transition region along the Cascadia megathrust influences coseismic behavior: insights from 2-D dynamic rupture simulations. Geophys. Res. Lett. 46, 1973–1983. https://doi.org/10.1029/2018GL080812.

Ripperger, J., Mai, P.M., Ampuero, J.P., 2008. Variability of near-field ground motion from dynamic earthquake rupture simulations. Bull. Seismol. Soc. Am. 98 (3), 1207–1228. https://doi.org/10.1785/0120070076.

Ramos, M.D., Huang, Y., Ulrich, T., Li, D., Gabriel, A.A., Thomas, A.M., 2021. Assessing margin-wide rupture behaviors along the Cascadia megathrust with 3-D dynamic rupture simulations. J. Geophys. Res., Solid Earth 126 (7), e2021JB022005.

Ruhl, C.J., Melgar, D., Geng, J., Goldberg, D.E., Crowell, B.W., Allen, R.M., et al., 2019. A global database of strong-motion displacement GNSS recordings and an example application to PGD scaling. Seismol. Res. Lett. 90 (1), 271–279.

Saffer, D.M., Tobin, H.J., 2011. Hydrogeology and mechanics of subduction forearcs: fluid flow and pore pressure. Annu. Rev. Earth Planet. Sci. 39 (1), 157–186.

Sahakian, V.J., Melgar, D., Muzli, M., 2019. Weak near-field behavior of a tsunami earthquake: toward real-time identification for local warning. Geophys. Res. Lett. 46 (16), 9519–9528.

Satake, K., Atwater, B.F., 2007. Long-term perspectives on giant earthquakes and tsunamis at subduction zones. Annu. Rev. Earth Planet. Sci. 35, 349–374.

Sgobba, S., Lanzano, G., Pacor, F., 2021. Empirical nonergodic shaking scenarios based on spatial correlation models: an application to central Italy. Earthq. Eng. Struct. Dyn. 50 (1), 60–80.

Small, D.T., Melgar, D., 2021. Geodetic coupling models as constraints on stochastic earthquake ruptures: an example application to PTHA in Cascadia. J. Geophys. Res., Solid Earth 126 (7), e2020JB021149.

Spudich, P., Chiou, B.S.J., 2008. Directivity in NGA earthquake ground motions: analysis using isochrone theory. Earthq. Spectra 24, 279–298.

Spudich, P., Rowshandel, B., Shahi, S.K., Baker, J.W., Chiou, B.S.-J., 2014. Comparison of NGA-West2 directivity models. Earthq. Spectra 30, 1199–1221.

Wang, K., Zhu, Y., Nissen, E., Shen, Z.-K., 2021. On the relevance of geodetic deformation rates to earthquake potential. Geophys. Res. Lett. 48, e2021GL093231. https://doi.org/10.1029/2021GL093231.

Weng, H., Yang, H., Zhang, Z., Chen, X., 2016. Earthquake rupture extents and coseismic slips promoted by damaged fault zones. J. Geophys. Res. https://doi.org/10.1002/2015JB012713.

Weng, H., Yang, H., 2018. Constraining frictional properties on fault by dynamic rupture simulations and near-field observations. J. Geophys. Res. 123 (8), 6658–6670. https://doi.org/10.1029/2017JB015414.

Xie, S., Dixon, T.H., Malservisi, R., Jiang, Y., Protti, M., Muller, C., 2020. Slow slip and Inter-transient locking on the Nicoya megathrust in the late and early stages of an earthquake cycle. J. Geophys. Res., Solid Earth 125, e2020JB020503. https://doi.org/10.1029/2020JB020503.

Xin, D., Zhang, Z., 2021. On the comparison of seismic ground motion simulated by physics-based dynamic rupture and predicted by empirical attenuation equations. Bull. Seismol. Soc. Am. 111 (5), 2595–2616. https://doi.org/10.1785/0120210077.

Xue, L., Schwartz, S., Liu, Z., Feng, L., 2015. Interseismic megathrust coupling beneath Nicoya Peninsula, Costa Rica, from the joint inversion of InSAR and GPS data. J. Geophys. Res. 120 (5), 3707–3722.

Yang, H., Liu, Y., McGuire, J., 2012a. Modeling rupture segmentations on the Cascadia megathrust. In: AGU Fall Meeting. S21B-2503.

Yang, H., Liu, Y., Lin, J., 2012b. Effects of subducted seamounts on megathrust earthquake nucleation and rupture propagation. Geophys. Res. Lett. 39, L24302. https://doi.org/10.1029/2012GL053892.

Yang, H., Yao, S., He, B., Newman, A.V., 2019a. Earthquake rupture dependence on hypocentral location along the Nicoya Peninsula subduction megathrust. Earth Planet. Sci. Lett. 520, 10–17. https://doi.org/10.1016/j.epsl.2019.05.030.

Yang, H., Yao, S., He, B., Newman, A.V., Weng, H., 2019b. Deriving rupture scenarios from interseismic locking distributions along the subduction megathrust. J. Geophys. Res. 124, 10376–10392. https://doi.org/10.1029/2019JB017541.

Yang, H., Wang, D., Guo, R., Xie, Mengyu, Zang, Y., 2022. Rapid report of the 8 January 2022 Ms 6.9 Menyuan earthquake, Qinghai, China. Earthqu. Res. Adv. (ISSN 2772-4670) 100113. https://doi.org/10.1016/j.eqrea.2022.100113.

Yao, S., Yang, H., 2022. Hypocentral dependent shallow slip distribution and rupture extents along a strike-slip fault. Earth Planet. Sci. Lett. (ISSN 0012-821X) 578, 117296. https://doi.org/10.1016/j.epsl.2021.117296.

Yao, S., Yang, H., 2020. Rupture dynamics of the 2012 Nicoya Mw 7.6 earthquake: evidence for low strength on the Megathrust. Geophys. Res. Lett. 47, e2020GL087508. https://doi.org/10.1029/2020GL087508.

Ye, L., Lay, T., Kanamori, H., 2013. Large earthquake rupture process variations on the Middle America megathrust. Earth Planet. Sci. Lett. 381, 147–155.

Yin, H., Wdowinski, S., 2014. Improved detection of earthquake-induced ground motion with spatial filter: case study of the 2012 M = 7.6 Costa Rica earthquake. GPS Solut. 18 (4), 563–570.

Yu, H., Liu, Y., Yang, H., Ning, J., 2018. Modeling earthquake sequences along the Manila subduction zone: effects of three-dimensional fault geometry. Tectonophysics 733, 73–84. https://doi.org/10.1016/j.tecto.2018.01.025.

Yue, H., Lay, T., Schwartz, S.Y., Rivera, L., Protti, M., Dixon, T.H., Owen, S., Newman, A.V., 2013. The 5 September 2012 Nicoya, Costa Rica Mw 7.6 earthquake rupture process from joint inversion of high-rate GPS, strong-motion, and teleseismic P wave data and its relationship to adjacent plate boundary interface properties. J. Geophys. Res., Solid Earth 118 (10), 5453–5466.

Zhang, Z., Zhang, W., Chen, X., Li, P., Fu, C., 2017. Rupture dynamics and ground motion from potential earthquakes around Taiyuan, China. Bull. Seismol. Soc. Am. 107, 1201–1212.